Physica Medica 133 (2025) 104971

Contents lists available at ScienceDirect

Physica Medica

journal homepage: www.elsevier.com/locate/ejmp

# Utilizing Pix2Pix conditional generative adversarial networks to recover missing data in preclinical PET scanner sinogram gaps

Zahra Karimi [a], Khadijeh Rezaee Ebrahim Saraee [a,*], Mohammad Reza Ay [b,c], Peyman Sheikhzadeh [b,d]

[a] Faculty of Physics, University of Isfahan, Isfahan, Iran
[b] Department of Medical Physics and Biomedical Engineering, School of Medicine, Tehran University of Medical Sciences, Tehran, Iran
[c] Research Center for Molecular and Cellular Imaging (RCMCI), Advanced Medical Technologies and Equipment Institute (AMTEI), Tehran University of Medical Sciences (TUMS), Tehran, Iran
[d] Department of Nuclear Medicine, IKHC, Faculty of Medicine, Tehran University of Medical Sciences, Tehran, Iran

ARTICLE INFO

*Keywords:*
Deep learning
PET scanner
Sinogram
Quantification

ABSTRACT

*Background:* The presence of a gap between adjacent detector blocks in Positron Emission Tomography (PET) scanners introduces a partial loss of projection data, which can degrade the image quality and quantitative accuracy of reconstructed PET images. This study suggests a novel approach for filling missing data from sinograms generated from preclinical PET scanners using a combination of an inpainting method and the Pix2Pix conditional generative adversarial network (cGAN).
*Materials and methods:* Twenty mice and Image Quality (IQ) phantom were scanned by a small animal Xtrim PET scanner, resulting in 7500 raw sinograms used for network training and test datasets. The absence of gap-free sinograms as the target for neural network training was a challenge. This issue was solved by artificially generating gap-free sinograms from the original sinogram. To assess the performance of the proposed approach, the sinograms were reconstructed using the ordered subset expectation maximization (OSEM) algorithm. The overall performance of the proposed network and the quality of the resulting images were quantitatively compared using various metrics, including the root mean squared error (RMSE), structural similarity index (SSIM), peak signal-to-noise ratio (PSNR), contrast-to-noise ratio (CNR), and signal-to-noise ratio (SNR).
*Results:* The Pix2Pix cGAN approach achieved an RMSE of $9.34 \times 10^{-4} \pm 5.7 \times 10^{-5}$ and an SSIM of $99.984 \times 10^{-2} \pm 1.8 \times 10^{-5}$, considering the corresponding inpainted sinograms as the target.
*Conclusion:* The proposed approach can retrieve missing sinogram data by learning a map derived from the whole sinogram compared to the adjacent pixels, which leads to better quantitative accuracy and improved reconstructed images.

## 1. Introduction

Small animal positron emission tomography (PET) scanners have become prominent due to the demand for animal models in biomedical research, such as preclinical pharmacology, genetics, and pathology studies [1]. The mechanical limitations in constructing PET scanners lead to a gap between two adjacent detector blocks, which is dominant in the acquired projection dataset, i.e., a sinogram [2]. Small gap regions in animal PET scanners account for more of the detection coverage area than large ring-diameter clinical PET machines. A gap of 17 mm has been shown to cause missing data for approximately 18 % of the data between two adjacent detector blocks in the ECAT high-resolution research tomography (HRRT) scanner. The presence of gap regions in projections noticeably diminishes the quantification accuracy of the reconstructed images, especially when using an analytical algorithm including filtered back-projection (FBP) [3]. This reduction may create streaking artifacts in the reconstructed image, which decreases the image's spatial resolution [4].

Prior literature has proposed various techniques for gap-filling in the sinogram domain to recover corrupted images. Various interpolation techniques before reconstruction [5–9], inpainting techniques [5,10], rotating the scanner gantry during data acquisition [11], data-adaptive

* Corresponding author.
*E-mail address:* kh.rezaee@ast.ui.ac.ir (K.R.E. Saraee).

https://doi.org/10.1016/j.ejmp.2025.104971
Received 23 June 2024; Received in revised form 25 March 2025; Accepted 26 March 2025
Available online 14 April 2025

filters in the transform domain (Discrete Cosine Transform (DCT) and Discrete Fourier Transform (DFT)) [2,11–15], constrained terms (such as wavelet and total variation) to reduce artifacts caused by gaps [16–20], compressed sensing (CS), a method of recovering images or signals from fewer measurements [10,21,22], dictionary learning [23], model-based algorithms [24–26], and techniques depending on the statistical framework, e.g., maximum likelihood expectation maximization (MLEM) or maximum a posterior (MAP) [4,8,27,28], have been proposed.

Interpolation methods may produce defective data in gap regions, resulting in secondary artifacts in the reconstructed image [15]. DCT is another method that removes the frequency generated through the gap by a suitable filter based on the inverse transform, resulting in a free gap sinogram. In addition, different scanners have specific gap patterns that require different frequency filters, thus making them inconvenient for practical use [2]. The success of all the approaches mentioned above is related to the number of gap regions that fail at a higher level of sparsity [29].

Over the last few years, deep learning (DL) methods have shown remarkable capabilities in medical image processing and analysis. These applications include noise reduction, metal artifact reduction, image reconstruction, region of interest segmentation and classification, computer-aided diagnosis (CADx), and prognosis [30,31]. Both generative adversarial networks (GANs) and convolutional neural networks (CNNs), deep learning models, are widely used in medical imaging. CNNs, developed in the 1980 s, are popular for visual recognition tasks. In contrast, GANs, introduced in 2014, were among the first models used for generative AI and can learn to create new data that follows a given pattern [31,32]. DL-based techniques have been demonstrated in several recent studies to fill the gap structure in PET sinogram data. Ground truth data was available in every instance to train the deep neural network; some focused on producing significant gaps as faulty detectors, while others created simulation data [3,4,29,33,34]. Inspired by these studies, we proposed a Pix2Pix conditional generative adversarial network (Pix2Pix cGAN) to retrieve and fill in missing data in preclinical PET sinograms caused by interblock gaps. Additionally, we modeled relatively significant gaps and applied this method [35]. According to some research, the Pix2Pix cGAN has potential in medical imaging, e.g., image denoising [36], segmentation [37], and other fields of image translation [38–42].

Therefore, this research aims to evaluate the feasibility of generating gap-free sinograms in a preclinical PET scanner to improve the image quality of preclinical PET scans using a Pix2Pix cGAN.

## 2. Material and methods

### *2.1. Scanner description*

Xtrim PET is a commercial scanner designed for small animal PET imaging in preclinical research [43]. The design, functionality, and performance of this system, as well as its readout electronics, have been thoroughly covered in separate publications [44–46]. In summary, It consists of 10 block detectors arranged in a precise decagon-like configuration with an inner diameter of 160 mm and a length of 50.2 mm along the axial direction. The axial and transaxial field of view are 50.3 mm and 100 mm, respectively. The block is composed of 24 × 24 arrays of Cerium-doped Lutetium Yttrium Orthosilicate (LYSO: Ce) scintillators, each measuring 2 × 2 × 10 $mm^3$ with a pixel pitch of 2.1 mm. These arrays are interfaced with 12 × 12 Silicon Photomultiplier (SiPM) pixels SiPM (Sensl ArrayC-30035-144P-PCB). There are 240 crystals in each detector ring and 5760 LYSO scintillation crystals housed within the gantry. The reflector material, Barium Sulphate ($BaSo_4$), with a thickness of 0.1 mm, was situated between the LYSO segments. Multiplexing boards, LYSO scintillators, and SiPM arrays are installed on the detector head. These parts are connected to the digital front-end (DFE) board by a flexible flat cable (FFC) and housed in a sturdy aluminum box. The DFE board is essential for recording and examining specific data about photon interaction. To measure the time pick-off of the event, the Leading Edge Discrimination (LED) algorithm was employed, and to determine the exact arrival time of annihilation photons, Time to digital converters (TDCs) was used [1,43,47].

This scanner obtains three-dimensional (3D) information in the coincidence list mode format (LMF), which includes the energy, timing, and spatial coordinates of incident photons within each detector block. After that, the detector block sends the data packet for every event to a Digital Coincidence Processing Unit (DCPU). The DCPU board separates random and prompt coincidences before sending them to the acquisition computer for additional processing and calibration. True events are histogrammed into 3D sinograms after applying positioning and energy corrections using pre-calculated look up tables (LUTs). Two-dimensional (2D) sinograms (256 × 256 × 47) were generated with the SSRB and Fourier rebinning (FORE) algorithms before reconstruction by software available to end users. For reconstructing 2D sinograms, an in-house reconstruction package is offered that includes the ordered subsets expectation maximization (OSEM) and filtered back projection (FBP) algorithms. A 128 × 128 × 47 or 256 × 256 × 47 matrix size is typically used to reconstruct images. The limited axial field-of-view in mice and rats necessitates the use of two-bed positions and three-bed positions for the acquisition of whole body images [43].

### *2.2. Experimental data sets*

#### *2.2.1. Physical phantom*

The NEMA NU-4 standards describe the image quality (IQ) phantom as a polymethyl-methacrylate cylinder with a diameter of 30 mm and a length of 50 mm. The phantom used to measure image quality metrics is composed of three distinct sections: two cold chambers filled with water and air, five replaceable rods with diameters ranging from 1 to 5 mm, and a homogeneous area for evaluating uniformity [43]. In this research, the IQ phantom was scanned via Xtrim PET three times for 20 min and was filled with $^{18}$F-FDG with an average activity of 3.7 MBq. Two of them were used for training, and the last one was used for the test dataset. The total phantom dataset included 180 raw 2D sinograms prior to data augmentation. Only the normalization process was performed on the obtained sinograms and reconstructed via the OSEM algorithm with 4 iterations and 4 subsets. The final images were 256 × 256 × 47 volume matrices and 0.78 × 0.78 × 1.05 $mm^3$ voxels with axial and transaxial fields of view set at 50.3 mm and 100 mm, respectively.

#### *2.2.2. Small animals*

In this study, the scan data of 20 mice (30 ± 10 g) were collected using small animal Xtrim PET. These mice were divided into two groups. Fifteen mice were chosen for training, and the remaining five mice were used for the test dataset. Each mouse was scanned for 10 min in 2-bed positions under anesthesia with an average activity of 12.95 ± 1.85 MBq of $^{18}$F-FDG. The 3D projection data were rebinned by the single-slice rebinning method (SSRB). The resulting dataset contained 2000 raw 2D sinograms before the data augmentation step. The sinograms were corrected only for normalization purpose. The OSEM algorithm was used to reconstruct the generated sinogram with 4 iterations and 4 subsets. The resulting images consisted of 256 × 256 × 47 volume matrices with 0.78 × 0.78 × 1.05 $mm^3$ voxels. Axial and transaxial fields of view were set at 50.3 mm and 100 mm, respectively.

### *2.3. Inpainting method*

To restore the gap region of the sinogram images, the technique of digital inpainting for reconstructing lost/damaged regions was employed [48]. Most inpainting methods work as follows: First, the image regions to be inpainted are chosen. The algorithm begins at the edge of the specified region, utilizing existing image data to complete the currently blank areas. This pixel is substituted with the normalized weighted average of all known neighboring pixels. More weight is given to the pixels close to the point, the border normal, and pixels on the boundary contours [45,49]. In this study, the sinogram's gap area was filled via inpainting method using an algorithm written in the Python programming language. Note that this functionality is not currently available in the software's latest version of Xtrim PET scan.

### 2.4. Data preparation for neural network

A significant obstacle in this research is the need for gap-free sinograms (accurate reference images) to train the neural network. This issue was resolved by generating ground truth data artificially from the original sinogram. First, the inpainting method filled the original gaps in the sinogram images and modified as the target. The width of the gap region in the original sinogram was approximately 3–5 pixels. Then, the artificial gaps were applied to the target sinograms with different widths (3, 4, and 5 pixels) similar to the original gap pattern, and their values became zero. These artificial gaps (referred to as the gap map) were added to the inpainted sinograms. These gaps were positioned across different locations, though consistently outside the regions previously filled by inpainting. The resulting data were used as input for the network, as shown in Fig. 1. This approach was developed to train the network using the original pixel data from the sinogram, rather than the values filled in by the inpainting process for the gaps and regardless of their placement. This process enabled the network to restore gap regions across the sinogram using reliable results. Moreover, artificial gaps of 15 pixels in width were added to the target sinograms to evaluate the effectiveness of the proposed algorithm for filling more significant gaps.

### 2.5. Data augmentation (2.2)

Data augmentation was performed during training to prevent the network from memorizing data [41]. Two methods were implemented to expand the quantity of data within the dataset. In the initial approach, the sinogram images were mirrored along the y-axis. In the alternate method, the elements of the array were moved horizontally along the x-axis, as shown in Fig. 1. Overall, 20 mouse and 3 phantom studies were expanded to include 7500 images.

### 2.6. Summation method

The summation method was introduced using the data obtained from the deep learning network while the original data remained unchanged. As previously mentioned, the sinogram image of the Xtrim PET scan contains gaps due to the space between the detector blocks. In this approach, the proposed network predicted the filled sinogram. Next, the filled regions were extracted and incorporated into the original sinogram. With this method, only the gap regions of the sinogram were filled with the proposed neural network, while the original data remained unchanged. This process was denoted as "Summation1″. Furthermore, this technique was applied to sinograms with more significant artificially added gaps, and this process was denoted as "Summation2.".

### 2.7. Deep network architecture

The image-to-image translation cGAN called pix2pix was implemented through the Keras and TensorFlow libraries using an NVIDIA GTX 1070Ti GPU. The cGAN is a variant of the GAN that uses labeled data for context, which helps the generator generate more accurate and focused output. Fig. 2 schematically demonstrates the proposed pix2pix cGAN model, which consists of two convolution networks: the generator and discriminator. The generator's 'U-Net' architecture includes an encoder and a decoder and connects them through a "skip connection". The skip connection allows for more stable learning than a straightforward encoder–decoder architecture. The encoder decreases the component of the input image by downsampling the feature map, and the decoder expands the component to generate a gap-free image by upsampling the extracted features. The generated images from the generator are then fed into a discriminator. The discriminator distinguishes a real image from the image created by the generator. The discriminator utilizes a convolutional PatchGAN classifier, which classifies images using patches of a specific size rather than the entire area.

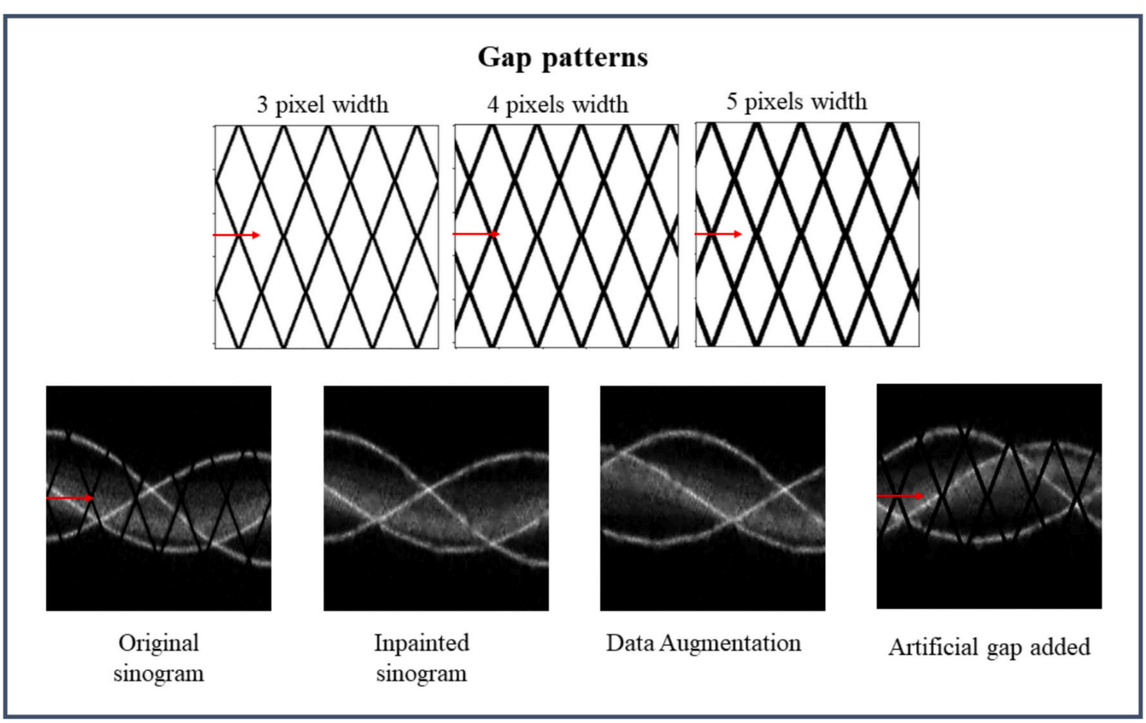


**Fig. 1.** The resultant gap patterns with different pixel widths, examples of inpainted sinogram, data augmentation from original sinogram, and artificial gaps added to inpainted sinogram.

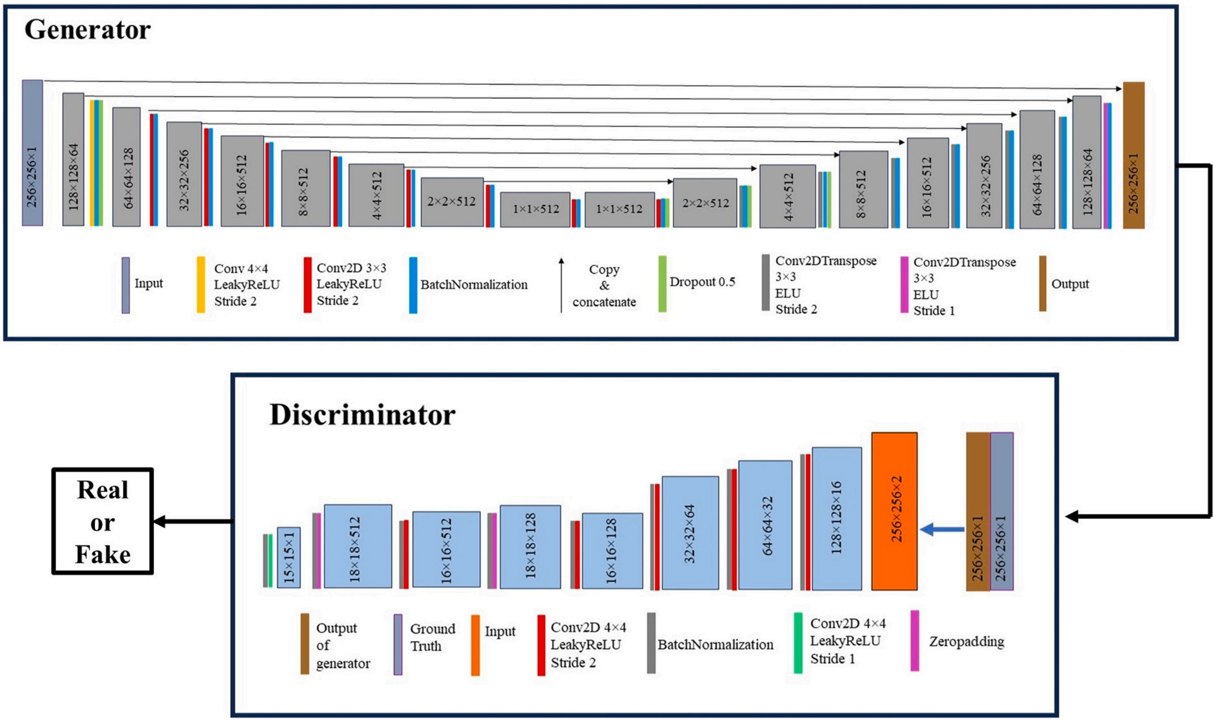


**Fig. 2.** Schematic illustration of the Pix2pix cGAN used in this study.

For both the generator and the discriminator, an Adam optimizer was applied with a nondecaying learning rate of 2e-4 and a beta of −1 to 0.5; moreover, the number of epochs was set to 30.

The trained cGAN model consists of two loss functions: the cGAN loss and the L1 loss. The cGAN loss functions when the discriminator tries to recognize the sinogram gap filled by the generator. The L1-Loss estimates the mean absolute error (MAE) between the generated gap-free sinogram and the ground truth image. The generator (G) was trained to convert the gapped sinogram (x) to a gapless sinogram (y) that is close to real samples. Furthermore, the discriminator (D) was trained to reduce the misclassification error of the gap-free sinogram and the gap-free image generated through the generator. This adversarial training is expressed as follows:

$$L_{GAN}(G,D) = E_{x,yp(x,y)}[logD(x,y)] + E_{xp(x)}[logD(x,G(x))] \tag{1}$$

In Eq. (1), $E_{x,yp(x,y)}$ represents the expected value when the gapped sinogram (x) and gap-free sinogram (y) are sampled in the probability distribution p(x, y). $E_{x,yp(x,y)}[logD(x,y)]$ is the maximum where D(x, y) = 1 because the discriminator (D) has an output between 0 and 1. The expected value of the gapped sinogram (x) for sampling from the probability distribution p(x) is denoted by $E_{xp(x)}$. $E_{xp(x)}[logD(x,G(x))]$ is maximized where $D(x,G(y)) = 0$ and is minimized where G is successfully deferred to D. As a result, $L_{GAN}(G,D)$ is maximized through the discriminator and is minimized through the generator.

L1-loss ($L_{L_1}$) in Eq. (2) is the MAE between the estimated output and the ground truth image.

$$L_{L_1}(G) = E_{x,yp(x,y)}\left[\|F - G(x)\|_1\right] \tag{2}$$

Combining two loss functions into one loss function effectively improves the quality of images produced by setting α to 100, an adjustable parameter, as expressed by Eq. (3) [36].

$$L = L_{GAN} + \alpha L_{L_1} \tag{3}$$

### 2.8. Analysis

The overall performance of the DL-based methods and image quality of the reconstructed images were quantitatively assessed by various quality metrics, including the root mean squared error (RMSE), structural similarity index (SSIM) [50], peak signal-to-noise ratio (PSNR), contrast-to-noise ratio (CNR) and signal-to-noise ratio (SNR). All images are displayed using the same scale.

The RMSE is the root mean square difference without dimension between the true values ($x_i$) and predicted values ($y_i$) for comparing the prediction errors (N is the pixel index of the input image). It is defined as follows:

$$RMSE(x,y) = \sqrt{\frac{1}{N}\sum_{i=1}^{N}(x_i - y_i)^2} \tag{4}$$

The SSIM is a perceptual metric for measuring image quality degradation caused by processing, such as loss in data transmission or data compression. It is based on the image's luminance, contrast, and structure calculated by Eq. (5) [51].

$$SSIM(x,y) = \frac{\left(2\mu_x\mu_y + c_1\right)\left(2\sigma_{xy}+c_2\right)}{\left(\mu_x^2 + \mu_y^2 + c_1\right)\left(\sigma_x^2 + \sigma_y^2 + c_2\right)} \tag{5}$$

where $\mu_x(\sigma_x^2)$ and $\mu_y(\sigma_y^2)$ are the means (variance) of the input image $x$ (estimates) and $y$ (ground truth), respectively. Here, $\sigma_{xy}$ is the covariance of $x$ and $y$, the variables $c_1 = (K_1L)^2$ and $c_2 = (K_2L)^2$ are the denominator stabilizers, $L$ is the dynamic range of the input pixel values, and $K_1$ and $K_2$ are set to 0.01 and 0.03 by default, respectively.

The PSNR is the ratio between the maximum possible signal power and the distorting noise power defined by Eq. (6). $y_{max}$ is the maximum value of the original image. MSE(x,y) is the mean square error of two input images ($MSE(x,y) = \frac{1}{N}\sum_{i=1}^{N}(x_i - y_i)^2$, where N in the pixel number of the input image).

$$PSNR(x,y) = 20log_{10}\left(\frac{y_{max}}{\sqrt{MSE(x,y)}}\right) \tag{6}$$

The CNR can be computed by Eq. (7). $L_{mean}$, $B_{mean}$ and $STD_B$ refer to the mean count in the lesion region of interest (ROI), the background

ROI, and the noise component as the standard deviation of the count within the background ROI, respectively [52].

$$CNR = \frac{L_{mean-B_{mean}}}{STD_B} \tag{7}$$

Another widely accepted metric, the SNR, can be calculated by Eq. (8). It is denoted as the ratio of the mean value ($L_{mean}$) to the standard deviation ($STD_B$) in the ROI in the lesion and background of the reconstructed image [53,54]. The ROIs corresponding to the targets were drawn as spherical shapes for CNR and SNR, and the same ROIs were placed inside the background medium. Four times, in different parts of the background, the ROIs were drawn, and the average of SNR and CNR were calculated.

$$SNR = \frac{L_{mean}}{STD_B} \tag{8}$$

The SNR and CNR differences between each method of gap filling (Pix2Pix, Summation1, Inpainted, Extra Gap and Summation2) and original data were estimated using paired T-test statistical method. In this approach, a P-value of less than 0.05 was considered statistically significant.

## 3. Results

Fig. 3 shows a plot of the proposed neural network's training loss and MAE for different numbers of epochs. These two curves generally tended to converge after 25 epochs, which indicates an increase in the network's ability to better represent its features. The Pix2Pix cGAN method achieved an RMSE of $9.34 \times 10^{-4} \pm 5.7 \times 10^{-5}$ and an SSIM of $99.984 \times 10^{-2} \pm 1.8 \times 10^{-5}$ when comparing the generated and ground truth images across all test slices.

Fig. 4 shows six variations of an axial slice of the mouse sinogram. The initial row pertains to the sinogram produced from the raw data of the Xtrim PET scan, the gap in the sinogram filled using pix2pix cGAN, the summation1 method, and the inpainted method, along with the inclusion of an artificial extra gap filled with generated pix2pix cGAN data (summation2). Deep learning and inpainted approaches could effectively compensate for the missing data. Furthermore, the Pix2Pix artificial neural network can generate a more precise and reliable filled gap. Fig. 4's second row shows the improvement in image quality due to gap filling when using the OSEM algorithm with 4 iterations and 4 subsets. The deep learning-based method provides better image quality than the other methods. However, the large gaps cause significant degradation in the reconstructed image. The third row contains the residual image, equal to the difference between the gap-filling images and the original image. The main difference between all the gap-filling images and the original image was the star-shaped artifact that was augmented with more gaps.

Fig. 5 shows the reconstructed images of the IQ phantom (two parts of chamber and uniform regions) via six methods. The difference between each reconstructed image and the corresponding original image was evaluated, and the results are shown in the row below. There is a noticeable star artifact and the most significant difference is associated with the additional gap. The original shape is significantly distorted as a result of his alteration, losing its intended clarity and design. The images produced using the Inpainted method display lower contrast and blurring around the edges of the shapes. Additionally, this method cannot eliminate the star artifact and demonstrates lower quantitative measurements compared to the Pix2Pix method. The Pix2Pix method could eliminate the star artifact compared to other methods with higher contrast and quantitative measurements.

In Fig. 6, six different types of reconstructed samples are shown. These include the original sinogram (first column), the test dataset of the Pix2Pix cGAN (second column), the summation1 (third column), the inpainted method (fourth column), the application of an extra gap (fifth column), and the summation2 (sixth column). The OSEM reconstruction method (4:4) was applied.

After evaluating six methods, the deep learning-based approach outperformed others by producing more desirable quality and detailed images. The remaining images closely resemble those generated by the deep learning method, as they show minimal variability in appearance. This is due to the low percentage of gap areas and the use of the reconstruction method. However, as the gap area increases, the differences between the reconstructed images become more noticeable. The following explanation explains the distinction between the images more clearly through quantitative measurements.

The quantitative results of the quality assessment indices, including the PSNR, RMSE, and SSIM, were reported for six methods compared to the original image. The PSNR, a metric for evaluating the quality of Pix2Pix and summation2, ranged from 29 to 36 dB, with a standard deviation of less than 0.001. However, this value was notably lower for the additional gap, particularly for image (a) at approximately 18.90 dB. The quality of the predicted images improves as the PSNR increases. The RMSE values were close to zero for pix2pix, summation1, and summation2 but increased to 0.27 for extra gaps. The RMSE exhibited a significant difference of approximately 45 % to 50 % between the inpainted and pix2pix values for images (a) and (e). The SSIM similarity metrics for the generated images were consistently above 0.92 across all datasets, with a standard deviation of less than 0.001, except for the extra gap images (a) and (c), which were below 0.90. Pix2pix and summation2

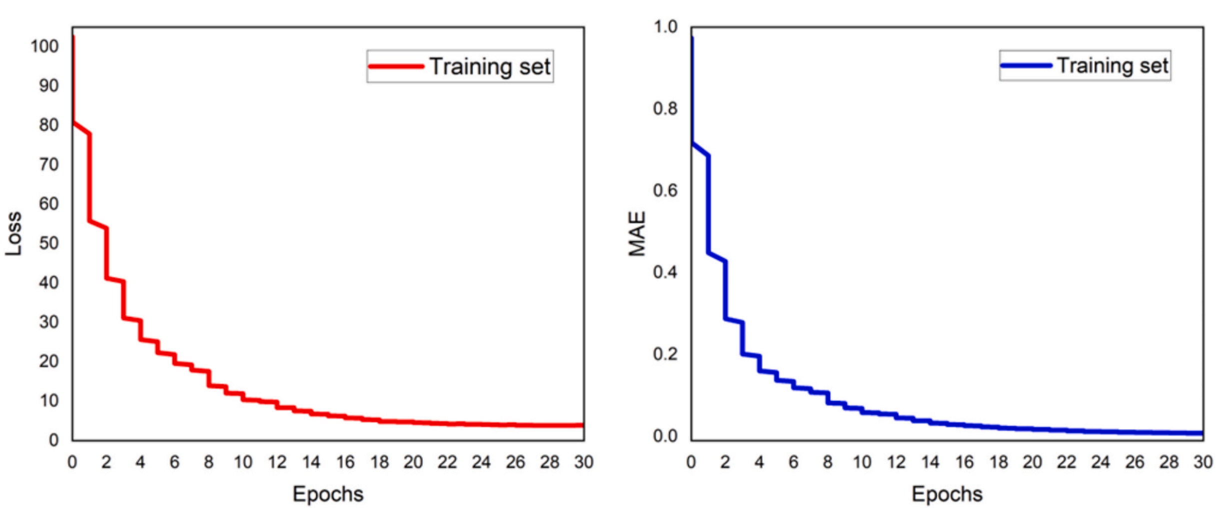


**Fig. 3.** The MAEs (a) and loss values (b) versus the number of epochs of the pix2pix cGAN from the training dataset.

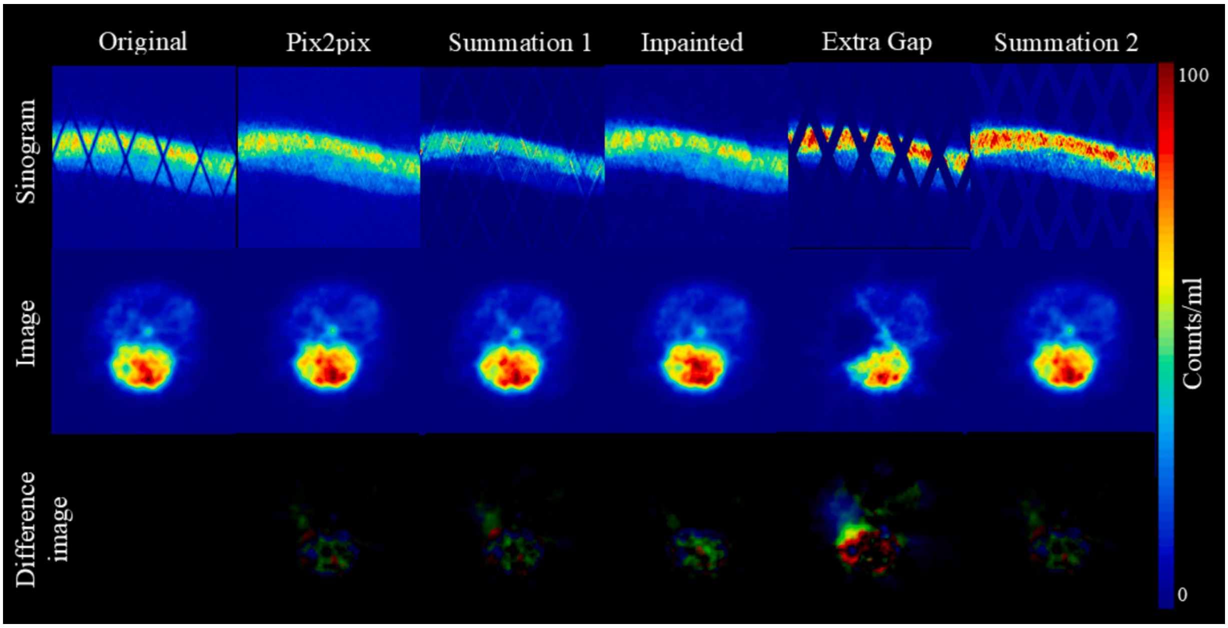


**Fig. 4.** A selective slice sinogram of a mouse with different gap-filling techniques and their reconstructed images with residual images between the original images. All the pictures are displayed with the same scale.

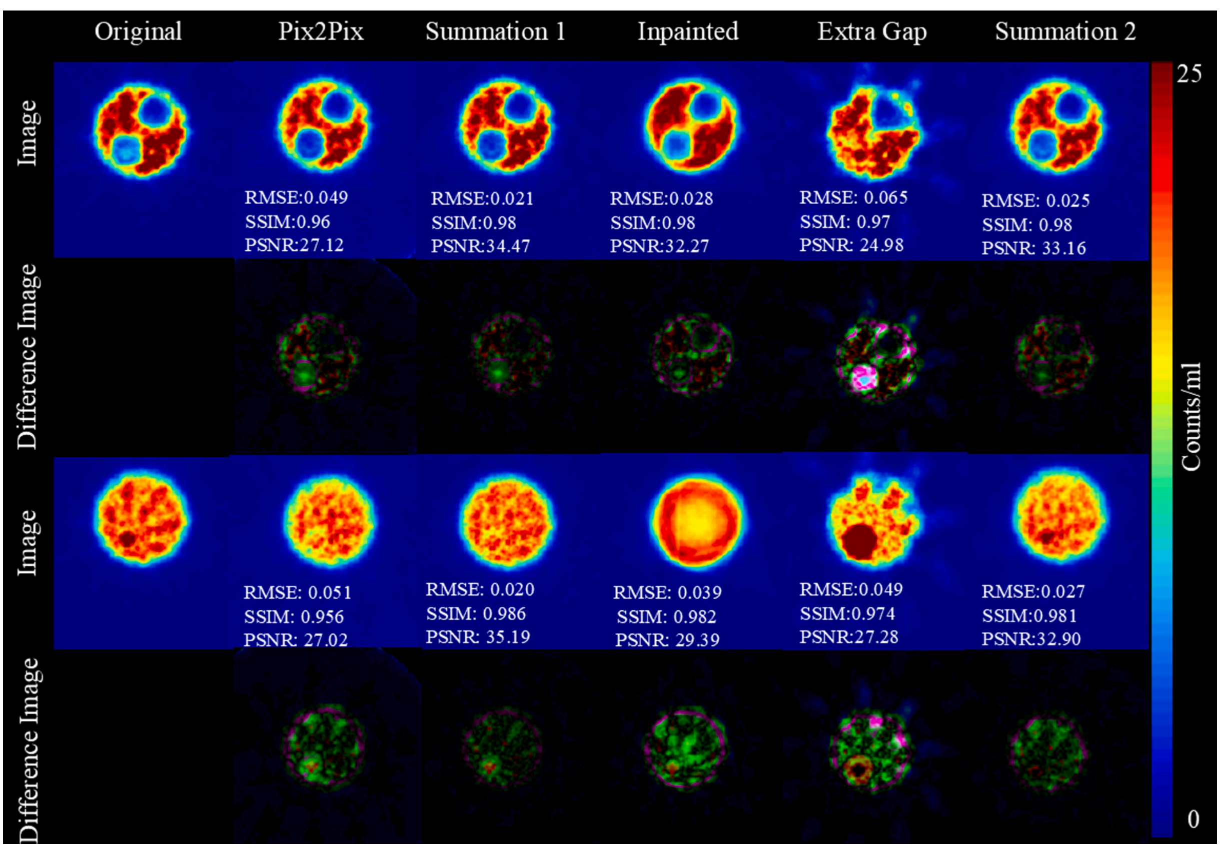


**Fig. 5.** Two selective slices of reconstructed images of an IQ phantom, using different gap-filling techniques and their corresponding residual images, are presented alongside the original images. All the pictures are displayed at the same scale.

outperformed the other methods in terms of image quality.

Additionally, Fig. 7 shows the image intensity profile extracted from the cross-sectional plane of the six test samples. The profile lines generated from the original, pix2pix, and summation2 methods had the most consistency with the slightest variation among all the samples, confirming the neural network's accuracy and effectiveness. However, the results of the extra gap, inpainted, and summation1 methods were inconsistent with those of the other three methods across all samples.

The performance of the SNR and CNR were reported in Table 1 via P-value. The T-test P-values reported for the six test sample images shown

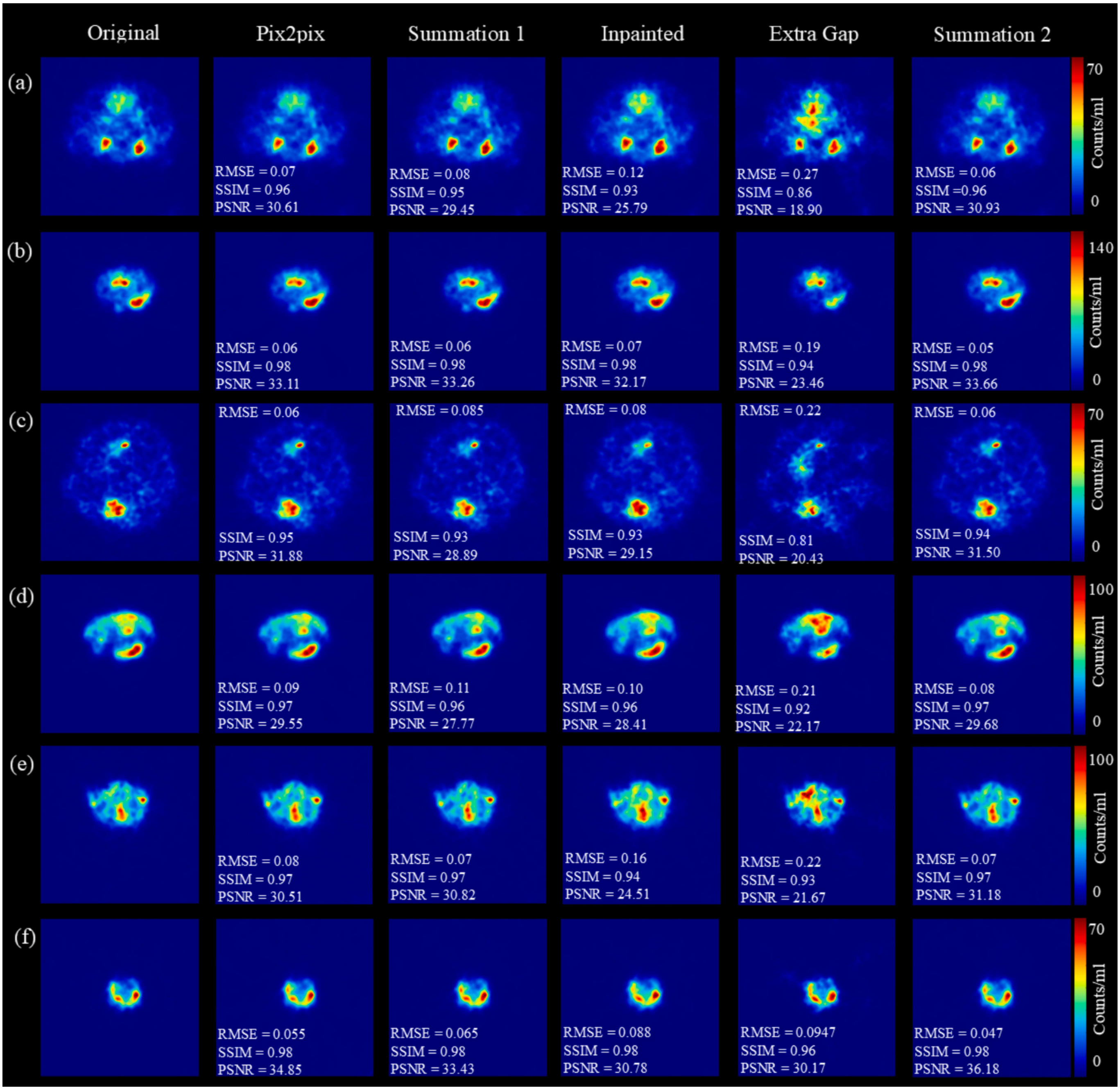


**Fig. 6.** Six test samples were reconstructed using the OSEM method from left to right: original data, Pix2Pix data, summation1, inpainted method, applying an extra gap, and summation2.

in Fig. 6 related to each method in comparison via original data. The results show that Pix2pix outperforms the other sampled images and approximately were statistically significant. The SNR and CNR for Summation1, Summation2, and Inpainted methods were not statistically significant. The Extra Gap method showed lower values compared to Pix2Pix, as evidenced by the images with a dominant star artifact.

## 4. Discussion

When there is a gap between adjacent detector blocks in a PET scanner, multiple areas in the detection field where data cannot be accurately captured are created. This can result in data loss and lower image quality in reconstruction processes.

This study introduces a DL-based method to address the issue of missing data caused by inter-detector gaps in the Xtrim PET scans. A considerable challenge in this study is the absence of ground truth data, which were artificially produced by the original sinogram. The inpainted method was used to fill the gap area in the original sinogram. Then, artificial gaps similar to the original pattern were created and located at different places except the inpainted area in the original sinogram. This method was implemented to help pix2pix learn the pattern of the gap map from the original data, focusing the network on the original sinogram data rather than the inpainted areas. While the inpainted area could contribute to training the proposed network, its contribution percentage is relatively low compared to the overall dataset, and it does not exist in the learning algorithm for filling the gaps in the network. Our findings indicate that pix2pix cGAN has the ability to learn to generate new data from a specific pattern and can potentially rectify

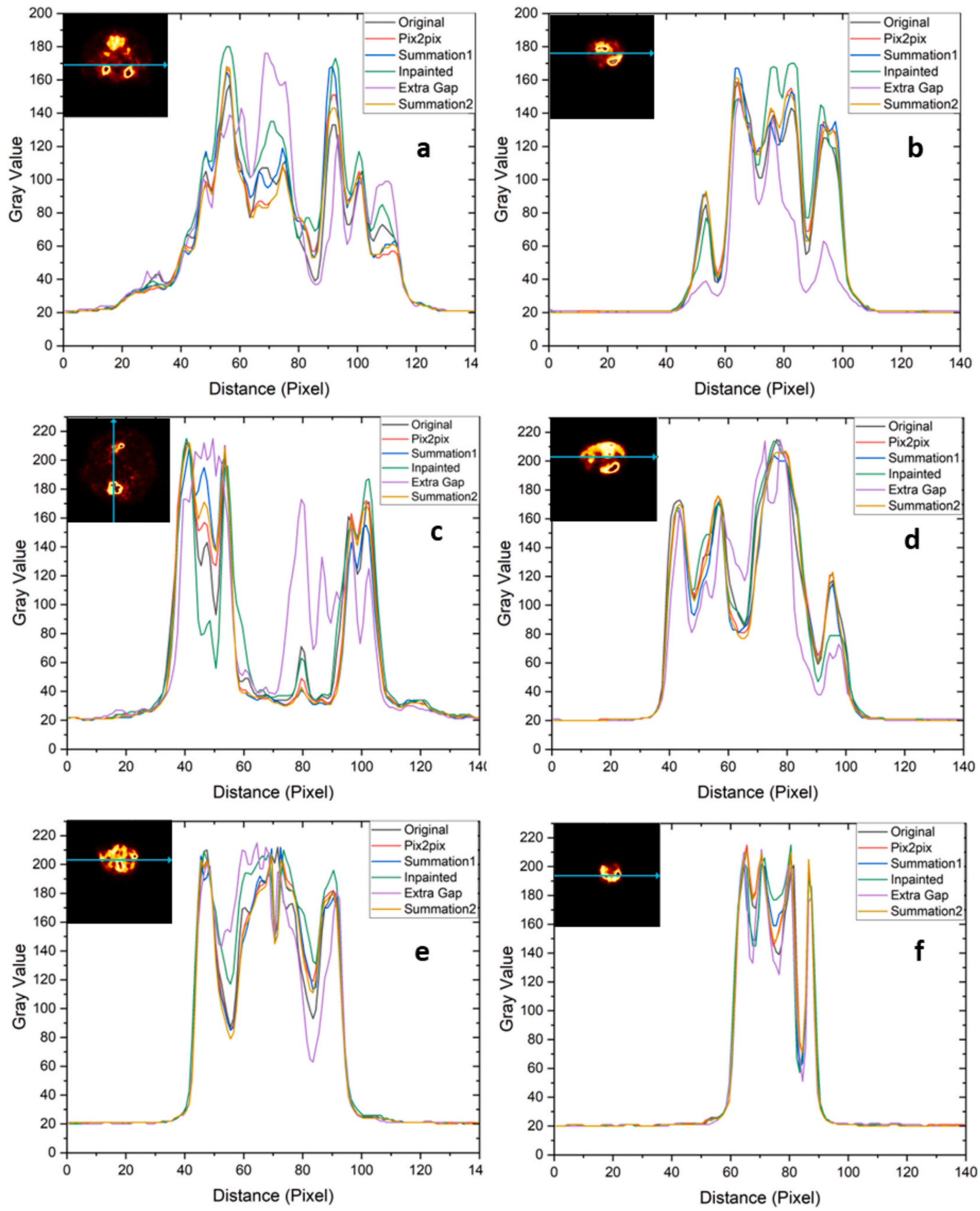


**Fig. 7.** A comparison of the profile lines of the six test samples were shown in Fig. 6.

**Table 1**
The CNRs and SNRs with P-value (each method via original data) for the six test sample images were shown in Fig. 6.

| | | Original | Pix2Pix | P-value | Summation1 | P-value | Inpainted | P-value | Extra Gap | P-value | Summation2 | P-value |
|---|---|---|---|---|---|---|---|---|---|---|---|---|
| a | CNR | 8.33 | 11.05 | 0.003 | 8.28 | 0.09 | 7.35 | 0.12 | 3.53 | 6E-04 | 10.02 | 0.017 |
| | SNR | 13.22 | 15.39 | 0.047 | 13.51 | 0.74 | 14.53 | 0.22 | 8.93 | 0.018 | 14.74 | 0.07 |
| b | CNR | 5.95 | 6.57 | 0.31 | 6.01 | 0.86 | 6.04 | 0.82 | 3.94 | 0.003 | 6.28 | 0.32 |
| | SNR | 12.30 | 14.15 | 0.001 | 12.65 | 0.601 | 13.27 | 0.37 | 8.57 | 0.003 | 13.45 | 0.048 |
| c | CNR | 12.04 | 12.20 | 0.83 | 11.94 | 0.88 | 11.35 | 0.51 | 8.83 | 0.005 | 11.70 | 0.75 |
| | SNR | 16.66 | 18.38 | 0.018 | 17.01 | 0.45 | 17.16 | 0.55 | 12.32 | 0.018 | 17.54 | 0.43 |
| d | CNR | 7.23 | 8.69 | 0.30 | 9.27 | 0.09 | 6.61 | 0.61 | 2.46 | 0.009 | 8.21 | 0.38 |
| | SNR | 13.24 | 15.48 | 0.08 | 14.69 | 0.19 | 12.95 | 0.83 | 5.54 | 2E-04 | 14.70 | 0.22 |
| e | CNR | 3.27 | 3.98 | 0.06 | 2.99 | 0.46 | 2.89 | 0.44 | 2.03 | 0.03 | 3.13 | 0.57 |
| | SNR | 10.10 | 11.22 | 0.009 | 10.49 | 0.07 | 11.59 | 0.29 | 7.32 | 0.012 | 10.64 | 0.024 |
| f | CNR | 4.14 | 6.85 | 0.018 | 3.83 | 0.57 | 2.73 | 0.077 | 2.51 | 0.02 | 5.19 | 0.12 |
| | SNR | 9.07 | 12.34 | 0.005 | 9.41 | 0.72 | 7.37 | 0.036 | 8.79 | 0.007 | 10.08 | 0.41 |

missing data in sinograms by acquiring knowledge of the data distribution and generating visually realistic approximated sinograms. In addition, the proposed DL-based network can substantially diminish noise and improve image quality with fewer artifacts [35].

The inpainting technique is used to restore missing areas of an image by utilizing data from surrounding pixels. However, this method typically concentrates on a local area to estimate the regions that need correction. This focus can lead to inconsistencies in the data, especially when dealing with larger gaps [5,10]. In this study, the sinograms had small gap areas, and the inpainted method's destructive effects were not clearly observed.

The reason for the slightly lower results of Summation1 compared to Pix2Pix was the worsening of the data inconsistency of the original data and Pix2Pix. In addition, the inpainted and extra gap methods decreased the image quality; nevertheless, the pix2pix method could generate a free gap sinogram and enhance the image quality.

Additionally, the quantitative results obtained in the picture of mice and IQ phantom were illustrate that the most suitable method for filling this gap is based on the DL-based approach. The reconstructed images of the IQ phantom were illustrated that the Pix2Pix method could generate the uniformly image without significant star artifact, good edge maintenance and noise suppression characteristics compared to other methods. The investigation of this proposed method on rat projections will also be considered for further complementary studies.

The significant artificial gaps were added to the original sinogram and filled with deep learning results to demonstrate the DL-based approach's feasibility better.

The OSEM reconstruction method was applied in this investigation. Although the FBP reconstruction method is advised by NEMA NU 4-2008, it introduces errors and artifacts that reduce spatial resolution. Additionally, systems with missing data or irregularly designed geometries cannot be subjected to the FBP method. Recently, iterative reconstruction techniques have become increasingly popular due to their ability to accurately model Poisson noise and the system response for PET image reconstruction [55].

Our findings have shown that the DL-based approach can generate high-quality and precise PET images on scanners. It is worth noting that the proposed method is very promising for different scanners with different configurations and for developing new PET scanner designs based on partial rings. Moving forward, we intend to further explore the capabilities and benefits of DL-based gap correction by comparing our results with those obtained from alternative methods.

## 5. Conclusion

Finally, we demonstrated and evaluated the proposed neural network, which learns a mapping from the entire sinogram in comparison to nearby pixels and provides a workable solution for restoring missing data in a sinogram. Comparing the reconstructed image to other introduced techniques, this approach also improved qualitative and quantitative outcomes.

## Ethical approval

We retrospectively collected the animal data for this research. The Ethics Committee of TUMS waived this in the ethics approval IR.TUMS.AED.1401.109.

## Declaration of competing interest

The authors declare that they have no known competing financial interests or personal relationships that could have appeared to influence the work reported in this paper.

## Acknowledgments

This work was partially funded by the Tehran University of Medical Sciences under Grant No. 62476. The authors acknowledge PNP Co. for their technical support.

## References

[1] Sanaat A, Zafarghandi MS, Ay MR. Design and performance evaluation of high resolution small animal PET scanner based on monolithic crystal: a simulation study. J Instrum 2019;14(01):P01005. https://doi.org/10.1088/1748-0221/14/01/P01005.
[2] Tuna U, Peltonen S, Ruotsalainen U. Gap-filling for the high-resolution PET sinograms with a dedicated DCT-domain filter. IEEE Trans Med Imaging 2010;29(3):830–9. https://doi.org/10.1109/TMI.2009.2037957.
[3] Huang Y, Zhu H, Duan X, Hong X, Sun H, Lv W, et al. Gapfill-recon net: a cascade network for simultaneously pet gap filling and image reconstruction. Comput Methods Programs Biomed 2021;208:106271. https://doi.org/10.1016/j.cmpb.2021.106271.
[4] Shiri I, Sheikhzadeh P, Ay MR. Deep-fill: Deep learning based sinogram domain gap filling in positron emission tomography. arXiv preprint arXiv 2019;1906.07168. doi: 10.48550/arXiv.1906.07168.
[5] Loukiala A, Tuna U, Beer S, Jahnke S, Ruotsalainen U. Gap-filling methods for 3D PlanTIS data. Phys Med Biol 2010;55(20):6125. https://doi.org/10.1088/0031-155/55/20/006.
[6] Tuna U, Peltonen S, Ruotsalainen U. Interpolation for the gap-filling of the HRRT PET sinograms by using the slices in the direction of the radial samples. IEEE Nuclear Science Symposium Conference Record 2009:3273–9. https://doi.org/10.1109/NSSMIC.2009.5401727.
[7] Peltonen S, Tuna U, Ruotsalainen U. 1-D interpolation method for the HRRT PET sinogram gap-filling. In: 2013 IEEE Nuclear Science Symposium and Medical Imaging Conference; 2013. p. 1–4. https://doi.org/10.1109/NSSMIC.2013.6829385.
[8] De Jong HWAM, Boellaard R, Knoess C, Lenox M, Michel C, Casey M, et al. Correction methods for missing data in sinograms of the HRRT PET scanner. IEEE Trans Nucl Sci 2002;50(5):1452–6. https://doi.org/10.1109/NSSMIC.2002.1239536.
[9] Tuna U, Johansson J, Ruotsalainen U. Evaluation of analytical reconstruction with a new gap-filling method in comparison to iterative reconstruction in_^11\mathrm C 11 C-raclopride PET studies. Ann Nucl Med 2014;28:417–29. https://doi.org/10.1007/s12149-014-0832-y.
[10] Shojaeilangari S, Schmidtlein CR, Rahmim A, Ay MR. Recovery of missing data in partial geometry PET scanners: compensation in projection space vs image space. Med Phys 2018;45(12):5437–49. https://doi.org/10.1002/mp.13225.
[11] Rodríguez-Villafuerte M, Yang Y, Cherry SR. A Monte Carlo investigation of the spatial resolution performance of a small-animal PET scanner designed for mouse brain imaging studies. Phys Med 2014;30(1):76–85. https://doi.org/10.1016/j.ejmp.2013.03.004.
[12] Tuna U, Peltonen S, Ruotsalainen U. Data estimation for the ECAT HRRT sinograms by utilizing the DCT domain. IEEE Nuclear Science Symposium Conference Record 2008:5076–80. https://doi.org/10.1109/NSSMIC.2008.4774379.
[13] Herraiz JL, Espana S, Vicente E, Herranz E, Desco M, Vaquero JJ, et al. Frequency selective signal extrapolation for compensation of missing data in sinograms. IEEE Nuclear Science Symposium Conference Record 2008:4299–302. https://doi.org/10.1109/NSSMIC.2008.4774234.
[14] Kim K, Lee K, Lee H, Joo S, Kang J. An iterative sinogram gap-filling method with object-and scanner-dedicated discrete cosine transform (DCT)-domain filters for high resolution PET scanners. Jpn J Radiol 2018;36(1):59–67. https://doi.org/10.1007/s11604-017-0697-9.
[15] Shih CT, Wu J, Lin HH, Chang SJ, Chuang KS. A novel adaptive discrete cosine transform-domain filter for gap-inpainting of high resolution PET scanners. Med Phys 2014;41:082501. https://doi.org/10.1118/1.4886035.
[16] Kisilev P, Zibulevsky M, Zeevi YY. Wavelet representation and total variation regularization in emission tomography. Int Conf Image Process 2001;1:702–5. https://doi.org/10.1109/ICIP.2001.959142.
[17] Jonsson E, Huang SC, Chan T. Total variation regularization in positron emission tomography. CAM Report 1998;9848.
[18] Lu L, Ma J, Feng Q, Chen W, Rahmim A. Anatomy-guided brain PET imaging incorporating a joint prior model. Phys Med Biol 2015;60(6):2145. https://doi.org/10.1088/0031-9155/60/6/2145.
[19] Bowsher JE, Johnson VE, Turkington TG, Jaszczak RJ, Floyd CE, Coleman RE. Bayesian reconstruction and use of anatomical a priori information for emission tomography. IEEE Trans Med Imaging 1996;15(5):673–86. https://doi.org/10.1109/42.538945.
[20] Wang G, Qi J. Penalized likelihood PET image reconstruction using patch-based edge-preserving regularization. IEEE Trans Med Imaging 2012;31(12):2194–204. https://doi.org/10.1109/TMI.2012.2211378.
[21] Valiollahzadeh S, Clark Jr JW, Mawlawi O. Using compressive sensing to recover images from PET scanners with partial detector rings. Med Phys 2015;42(1):121–33. https://doi.org/10.1118/1.4903291.
[22] Ahn S, Kim SM, Son J, Lee DS, Sung LJ. Gap compensation during PET image reconstruction by constrained, total variation minimization. Med Phys 2012;39(2):589–602. https://doi.org/10.1118/1.3673775.

[23] Valiollahzadeh S, Clark JW, Mawlawi O. Dictionary learning for data recovery in positron emission tomography. Phys Med Biol 2015;60(15):5853. https://doi.org/10.1088/0031-9155/60/15/5853.
[24] Karp JS, Muehllehner G, Lewitt RM. Constrained Fourier space method for compensation of missing data in emission computed tomography. IEEE Trans Med Imaging 1988;7(1):21–5. https://doi.org/10.1109/42.3925.
[25] Ren R, Li Q, Ahn S, Cho S, Leahy RM. Estimation of gap data using bow-tie filters for 3D time-of-flight PET. IEEE Nuclear Science Symposuim & Medical Imaging Conference 2010:2691–4. https://doi.org/10.1109/NSSMIC.2010.5874279.
[26] Baghaei H, Li H, Zhang Y, Ramirez RA, Liu S, Wang C, et al. An evaluation of missing data compensation methods for a PET camera by comparing to no-gap data. IEEE Nuclear Science Symposium Conference Record 2008:5273–6. https://doi.org/10.1109/NSSMIC.2008.4774424.
[27] Kinahan PE, Fessler JA, Karp JS. Statistical image reconstruction in PET with compensation for missing data. IEEE Trans Nucl Sci 1997;44(4):1552–7. https://doi.org/10.1109/23.632729.
[28] Nguyen VG, Lee SJ. Image reconstruction from limited-view projections by convex nonquadratic spline regularization. Opt Eng 2010;49(3):037001. https://doi.org/10.1117/1.3339871.
[29] Amirrashedi M, Sarkar S, Ghadiri H, Ghafarian P, Zaidi H, Ay MR. A deep neural network to recover missing data in small animal pet imaging: comparison between sinogram-and image-domain implementations. In: IEEE 18th International Symposium on Biomedical Imaging (ISBI); 2021. p. 1365–8. https://doi.org/10.1109/ISBI48211.2021.9433923.
[30] Shen D, Wu G, Suk HI. Deep learning in medical image analysis. Annu Rev Biomed Eng 2017;19:221–48. https://doi.org/10.1146/annurev-bioeng-071516-044442.
[31] Arabi H, AkhavanAllaf A, Sanaat A, Shiri I, Zaidi H. The promise of artificial intelligence and deep learning in PET and SPECT imaging. Phys Med 2021;83:122–37. https://doi.org/10.1016/j.ejmp.2021.03.008.
[32] Li Z, Cai A, Wang L, Zhang W, Tang C, Li L, et al. Promising generative adversarial network based sinogram inpainting method for ultra-limited-angle computed tomography imaging. Sensors 2019;19(18):3941. https://doi.org/10.3390/s19183941.
[33] Liu CC, Huang HM. Partial-ring PET image restoration using a deep learning based method. Phys Med Biol 2019;64(22):225014. https://doi.org/10.1088/1361-6560/ab4aa9.
[34] Whiteley W, Gregor J. CNN-based PET sinogram repair to mitigate defective block detectors. Phys Med Biol 2019;64(23):235017. https://doi.org/10.1088/1361-6560/ab4919.
[35] Isola P, Zhu JY, Zhou T, Efros AA. Image-to-image translation with conditional adversarial networks. Proceedings of the IEEE conference on computer vision and pattern recognition 2017:1125–34.
[36] Sun J, Du Y, Li C, Wu TH, Yang B, Mok GS. Pix2Pix generative adversarial network for low dose myocardial perfusion SPECT denoising. Quant Imaging Med Surg 2022;12(7):3539. https://doi.org/10.21037/qims-21-1042.
[37] Oh KT, Lee S, Lee H, Yun M, Yoo SK. Semantic segmentation of white matter in FDG-PET using generative adversarial network. J Digit Imaging 2020;33(4):816–25. https://doi.org/10.1007/s10278-020-00321-5.
[38] Jung MM, van den Berg B, Postma E, Huijbers W. Inferring PET from MRI with pix2pix. In Benelux Conference on Artificial Intelligence 2018;vol. 9.
[39] Fujioka T, Satoh Y, Imokawa T, Mori M, Yamaga E, Takahashi K, et al. Proposal to improve the image quality of short-acquisition time-dedicated breast positron emission tomography using the pix2pix generative adversarial network. Diagnostics 2022;12(12):3114. https://doi.org/10.3390/diagnostics12123114.
[40] Hosch R, Weber M, Sraieb M, Flaschel N, Haubold J, Kim MS, et al. Artificial intelligence guided enhancement of digital PET: scans as fast as CT? Eur J Nucl Med Mol Imaging 2022;49(13):4503–15. https://doi.org/10.1007/s00259-022-05901-x.
[41] Ghafari A, Sheikhzadeh P, Seyyedi N, Abbasi M, Farzenefar S, Yousefirizi F, et al. Generation of 18F-FDG PET standard scan images from short scans using cycle-consistent generative adversarial network. Phys Med Biol 2022;67(21):215005. https://doi.org/10.1088/1361-6560/ac950a.
[42] Tahri S, Barateau A, Cadin C, Chourak H, Ribault S, Nozahic F, et al. A high-performance method of deep learning for prostate MR-only radiotherapy planning using an optimized Pix2Pix architecture. Phys Med 2022;103:108–18. https://doi.org/10.1016/j.ejmp.2022.10.003.
[43] Amirrashedi M, Sarkar S, Ghafarian P, Hashemi Shahraki R, Geramifar P, Zaidi H, et al. NEMA NU-4 2008 performance evaluation of Xtrim-PET: a prototype SiPM-based preclinical scanner. Med Phys 2019;46(11):4816–25. https://doi.org/10.1002/mp.13785.
[44] Zeraatkar N, Sajedi S, Kaviani S, et al. Development of a preclinical PET system based on pixelated LYSO crystals and SiPM arrays. In: IEEE Nuclear Science Symposium and Medical Imaging Conference (NSS/ MIC); 2017. https://doi.org/10.1109/NSSMIC.2017.8532985.
[45] Sajedi S, Zeraatkar N, Taheri M, et al. Generic high resolution PET detector block using 12 9 12 SiPM array. Biomed Phys Eng Express 2018;4:035014. https://doi.org/10.1088/2057-1976/aaade8.
[46] Sajedi S, Zeraatkar N, Taheri M, et al. A generic, scalable, and cost effective detector front-end block for PET. In: IEEE Nuclear Science Symposium and Medical Imaging Conference (NSS/MIC); 2017. https://doi.org/10.1109/NSSMIC.2017.8532917.
[47] Sheikhzadeh P, Sabet H, Ghadiri H, Geramifar P, Ghafarian P, Ay MR. Design, optimization and performance evaluation of BM-PET: a simulation study. Nucl Instrum Methods Phys Res Sect A 2019;940:274–82. https://doi.org/10.1016/j.nima.2019.05.083.
[48] Telea A. An image inpainting technique based on the fast marching method. J Graphics tools 2004;9(1):23–34. https://doi.org/10.1080/10867651.2004.10487596.
[49] Guillemot C, Le Meur O. Image inpainting: overview and recent advances. IEEE Signal Process Mag 2013;31(1):127–44. https://doi.org/10.1109/MSP.2013.2273004.
[50] Wang Z. Image quality assessment: form error visibility to structural similarity. IEEE Trans Image Process 2004;13(4):604–6.
[51] Setiadi DRIM. PSNR vs SSIM: imperceptibility quality assessment for image steganography. Multimed Tools Appl 2021;80(6):8423–44. https://doi.org/10.1007/s11042-020-10035-z.
[52] Koç A, Güveniş A. Design and evaluation of an accurate CNR-guided small region iterative restoration-based tumor segmentation scheme for PET using both simulated and real heterogeneous tumors. Med Biol Eng Comput 2020;58:335–55. https://doi.org/10.1007/s11517-019-02094-8.
[53] Yan J, Schaefferkoetter J, Conti M, Townsend D. A method to assess image quality for low-dose PET: analysis of SNR, CNR, bias and image noise. Cancer Imaging 2016;16:1–12. https://doi.org/10.1186/s40644-016-0086-0.
[54] Arabi H, Zaidi H. Spatially guided nonlocal mean approach for denoising of PET images. Med Phys 2020;47(4):1656–69. https://doi.org/10.1002/mp.14024.
[55] Gong K, Cherry SR, Qi J. On the assessment of spatial resolution of PET systems with iterative image reconstruction. Phys Med Biol 2016;61(5):N193. https://doi.org/10.1088/0031-9155/61/5/N193.